Materials & Design 260 (2025) 115227

Contents lists available at ScienceDirect

Materials & Design

journal homepage: www.elsevier.com/locate/matdes

Structure-property-bioresponse correlation in Zr-based metallic glasses: from glass-forming ability to corrosion resistance and gene expression

Fereshteh Sourani [a,*], Parthiban Ramasamy [a], Elham Sharifikolouei [b], Christoph Gammer [a], Alessandro Scalia [b], Tiziana Brosio [b], Andrea Cochis [b], Lia Rimondini [b], Jürgen Eckert [a,c]

[a] Erich Schmid Institute of Materials Science, Austrian Academy of Sciences, Jahnstraße 12, A-8700 Leoben, Austria
[b] Department of Health Sciences, Center for Translational Research on Autoimmune and Allergic Diseases–CAAD, Università Del Piemonte Orientale UPO, Corso Trieste 15/A, 28100 Novara, NO, Italy
[c] Department of Materials Science, Montanuniversitat Leoben, Jahnstraße 12, A-8700 Leoben, Austria

ARTICLE INFO

Keywords:
Zr-based metallic glasses
Glass-forming ability
Structural properties
Corrosion behavior
Cytocompatibility and Inflammation

ABSTRACT

Demand for orthopedic and dental implants continues to grow, driven by an aging population and traumatic injuries. Although current implant alloys have achieved clinical success, challenges related to ion release, inflammation, and long-term durability persist. To address these concerns, we developed three novel, biocompatible Zr-based metallic glasses free of toxic elements: $Zr_{66.5}Pd_{16.5}Al_{10}Fe_5Ti_2$, $Zr_{66.5}Pt_{16.5}Al_{10}Fe_5Ti_2$, and $Zr_{66.5}Au_{16.5}Al_{10}Fe_5Ti_2$, fabricated via melt spinning. Their glass-forming ability, structural, thermal, and electrochemical properties were systematically evaluated, demonstrating high thermal stability and corrosion resistance suitable for biomedical applications, and indicating their potential use as intramedullary implants. Cytocompatibility was assessed by exposing human bone-marrow-derived mesenchymal stromal cells to alloy supernatants, which showed no adverse effects on metabolic activity or viability. The inflammatory response was investigated by analyzing COX2, PTGES2, and VEGF expression in human gingival fibroblasts. Notably, despite the conventional classification of Pd and Pt ions as pro-inflammatory, both Pd- and Pt-containing alloys downregulated inflammatory markers, similar to Au-containing alloys. These results indicate that immune modulation depends not only on elemental identity but also on ion release kinetics and structural context. Taken together, the results demonstrate that integrating corrosion behavior, cytocompatibility, and molecular assays provides a coherent framework for the rational design of immunologically safe metallic-glass implants.

1. Introduction

Ni-free Zr-based bulk metallic glasses (BMGs) have recently attracted increasing interest because their amorphous structure provides high strength, low Young's modulus, good fatigue resistance, and favorable biocompatibility [1–4]. These qualities make them suitable candidates for biomedical uses such as osteosynthesis devices and load-bearing implants [2,5,6]. However, many Zr-based alloys with high glass-forming ability (GFA) still include Be, Ni, Co, or Cu, which can cause allergic reactions or cytotoxic effects [7]. Although there has been notable progress, most previous studies have focused on GFA and mechanical properties, while the long-term biological effects, particularly the inflammatory responses induced by corrosion and ion release, remain insufficiently characterized [8,9]. This gap highlights the need for an integrated approach that connects structural properties with biological performance in developing next-generation biomaterials.

One promising approach is to develop Ni- and Cu-free compositions that preserve the benefits of Zr-based BMGs while removing toxic elements. In this context, Zr-Al-Fe metallic glasses (MGs) and BMGs are attractive candidates because their composition excludes Ni and Cu, thereby reducing the risk of cytotoxic or inflammatory responses. Additionally, Fe addition helps lower production costs [10]. The Zr-Al-Fe system also facilitates modeling and exploration of composition–property relationships in MGs [11]. In particular, Zr-rich alloys (>65 at. % Zr) are attractive because they offer greater compositional flexibility and enhanced resistance to annealing-induced embrittlement compared to traditional Zr-based alloys (~50 at.% Zr). These features make Zr-rich BMGs especially promising for biomedical applications. For instance, Jin et al. [12] described a $Zr_{58}Al_{12}Fe_8Cu_{22}$ alloy within the Zr-Al-Fe-Cu system that achieved a 13 mm critical diameter. Similarly, Inoue et al.

* Corresponding author.
E-mail address: Fereshteh.sourani@oeaw.ac.at (F. Sourani).

https://doi.org/10.1016/j.matdes.2025.115227
Received 26 July 2025; Received in revised form 19 November 2025; Accepted 25 November 2025
Available online 27 November 2025

[13] developed $Zr_{60}Al_{10}Fe_5Cu_{25}$ and $Zr_{62.5}Al_{10}Fe_5Cu_{22.5}$ alloys with a 20 mm casting diameter. Although these alloys exhibit excellent GFA, their limited room-temperature plasticity continues to restrict their biomedical applications.

To overcome these limitations, alloying with small amounts of Ag [14,15], Ti [15], and Nb [16] has been extensively investigated. Among these elements, Ti is particularly effective, as it improves GFA, fracture resistance, and plasticity. As a bioinert element with excellent corrosion resistance, Ti is also well suited for permanent implants [17]. Han et al. [18] developed $Zr_{60.5}Ti_3Al_9Fe_{4.5}Cu_{23}$ BMG, which combined strong GFA, good mechanical properties, and biocompatibility, making it a promising biomedical candidate. Shi et al. [19] produced a $Zr_{65-x}Ti_xCu_{20}Al_{10}Fe_5$ (x = 0, 2, 4, 6, and 8) series of alloys, among which $Zr_{63}Ti_2Cu_{20}Al_{10}Fe_5$ exhibited the widest supercooled liquid region (73 K), along with high strength (1905 MPa) and plasticity (8.57 %). In comparison, the reference $Zr_{65}Cu_{20}Fe_5Al_{10}$ BMG shows values of 67 K and 1854 MPa. Nb has likewise been reported to enhance GFA, corrosion resistance, strength, and plasticity in many BMG systems [20–23]. Despite these advances, no widely adopted commercially viable alloy has yet satisfied the combined requirements of high GFA, strength, corrosion resistance, and immune compatibility. Representative systems include Zr-Al-Cu-Fe [12], Zr-Cu-Pd-Al-Nb [24], and Zr-Al-Cu-Fe-(Ti/Nb) [25], which show high GFA and biocompatibility comparable to the gold-standard Ti-6Al-4 V alloy. However, these alloys still suffer from inadequate mechanical performance and limited corrosion resistance [26]. In particular, Ni- and Cu-free compositions often exhibit insufficient corrosion resistance and limited immunomodulatory potential for clinical translation. Biocompatible Zr-Al-Fe BMGs have shown enhanced plasticity [25], their clinical application remains limited. This limitation is often caused by the deep eutectic nature of such alloys, which improves GFA but reduces corrosion resistance. For instance, Ni-free Zr-Al-Co BMGs have been developed, although further optimization is necessary. Focusing on only biocompatible elements represents a promising route toward creating long-term implant alloys [27,28]. Experimental studies also show that Cu can induce oxidative stress and inflammatory responses, as demonstrated in zebrafish models [29]. Even low levels of Cu ion release (~250 ppm) have been reported to cause cytotoxicity [28], posing serious risks for load-bearing implants. In this regard, only a few studies have explored Zr-based MGs with reduced Cu content. Reported low-Cu systems, such as $Zr_{61}Al_{8.9}Fe_{10.2}Cu_{10.2}Ag_{9.7}$ and $Zr_{60.5}Al_{8.9}Fe_{10.2}Cu_{10.2}Ag_{9.7}Ti_{0.5}$, demonstrate high strength (greater than 3×10^5 $N{\cdot}m{\cdot}kg^{-1}$), reduced Young's modulus (~80 GPa), and measurable plasticity (above a certain percentage), along with favorable biocompatibility. However, systematic evaluations of their tribological behavior, corrosion, and cytotoxicity remain limited [30,31].

Although cytotoxicity is an important factor in implant screening, recent research shows it does not fully reflect the biological performance of implants. Inflammatory responses, which are crucial for early implant integration and long-term healing, are affected not only by alloy composition but also by corrosion-driven ion release and the amorphous structure [9]. While ions such as Cu^{2+}, Pd^{2+}, and Pt^{2+} are often associated with pro-inflammatory signaling [8,32], most evidence originates from crystalline materials or salts. In contrast, the corrosion and ion-leaching behavior of MGs under physiological conditions may elicit distinct immune responses [33]. Connecting inflammatory markers to corrosion behavior is therefore essential for understanding the actual biological effects of candidate MGs and for creating a more predictive and biologically grounded framework for implant design. To address these limitations, this study proposes a targeted approach by designing Zr-based MGs in which Cu is replaced with biocompatible precious metals (Pd, Pt, Au). Our method combines thermodynamic modeling with systematic evaluation of corrosion, cytocompatibility, and inflammatory gene expression, thereby developing a comprehensive structure–property–bioresponse framework for the rational design of next-generation implants [34,35].

Accordingly, the objectives of this work are: (i) to develop Ni- and Cu-free Zr-based MGs with improved GFA, (ii) to evaluate their thermal, mechanical, and electrochemical stability, and (iii) to correlate their corrosion-driven ion release with cytocompatibility and inflammatory gene expression. Through this integrated approach, we aim to identify immunologically safe and durable candidate alloys for biomedical implants. The compositions were chosen because Pd, Pt, and Au can replace Cu while maintaining strong GFA [7,34]. These noble metals also offer additional benefits, such as highly negative mixing enthalpies with Zr, which further promote glass formation. The Zr-(Pd/Pt/Au)-Al-Fe-Ti alloys also meet Inoue's three empirical criteria, demonstrating high potential for glass formation. Moreover, they lower the liquidus temperature (T_l) of Zr (1855 °C), with reported eutectic temperatures of 1345 K, 1458 K, and 1378 K for Zr-Pd, Zr-Pt, and Zr-Au, respectively [29,30,35]. Among these elements, Pd-based alloys are extensively employed in dental applications, with strong evidence supporting their safety. Although some studies report allergenic or toxic effects, Pd is generally considered one of the least harmful metallic ions, demonstrating low chemical reactivity in alloys and rarely being released in large amounts. These attributes make Pd a suitable and stable alloying element for biomedical applications [36].

Finally, this study evaluates thermodynamic parameters, specifically P_{HS} ($\Delta H^C(\Delta S_\sigma/k_B)$) and P_{HSS} ($P_{HS} \times (\Delta S_C/R)$), which are derived from chemical mixing enthalpy, mismatch entropy, and configurational entropy. These metrics guide improvements in the GFA of the designed alloys. Additionally, we analyze how ion release affects early inflammatory signaling, thereby providing a more biologically relevant perspective to their evaluation.

2. Materials and methods

2.1. Sample preparation

Master alloys with nominal compositions (at.%) of $Zr_{66.5}Cu_{16.5}Al_{10}Fe_5Ti_2$ (ZAFT-Cu), $Zr_{66.5}Pd_{16.5}Al_{10}Fe_5Ti_2$ (ZAFT-Pd), $Zr_{66.5}Pt_{16.5}Al_{10}Fe_5Ti_2$ (ZAFT-Pt), and $Zr_{66.5}Au_{16.5}Al_{10}Fe_5Ti_2$ (ZAFT-Au) were produced by arc melting (AM/0.5-Edmund Bühler) from high-purity elements Zr (99.20 %), Al (99.90 %), Fe (99.99 %), Ti (99.90 %), Pd (99.99 %), Pt (99.9 %), Cu (99.9 %), Au (99.995 %) under a Ar atmosphere (99.999 %) at a base pressure of approximately 5×10^{-60} mbar. The ingots were remelted repeatedly (four times) to achieve a high homogeneity. The alloys were ejected at a temperature 100 K above their liquidus temperature. The copper wheel velocity was maintained at 31.4 m/s. Quartz crucibles with an orifice of approximately 1 mm were used for melting and ejection. The resulting ribbons all had a uniform width of ~4 mm and thickness as follows:32 ± 1 μm for ZAFT-Cu, ~38 ± 5 μm for ZAFT-Pd, ~40 ± 3 μm for ZAFT-Pt, and ~26 ± 2 μm for ZAFT-Au alloys.

2.2. Structural, thermal, and electrochemical characterization

Structural characterization of the as-spun ribbons was performed using X-ray diffraction (XRD) on a Bruker D2 Phaser equipped with Co Kα radiation (λ = 0.17889 nm) and a grazing incidence angle of 1°. To further assess the alloy structure, transmission electron microscopy (TEM; JEOL 2200FS FEG) was conducted at 200 kV. High-resolution TEM (HRTEM) micrographs and selected area electron diffraction (SAED) patterns were captured. A precision ion polishing system (PIPS) operating with Ar^+ ion milling was used to prepare the TEM samples. Typically, ion energies of 1–6 keV are used for polishing, with lower energies (1–2 keV) applied during final thinning to reduce sample damage.

A Netzsch DSC 404 F1 Pegasus device was used for Differential Scanning Calorimetry (DSC) analysis at a heating rate of 20 K/min under a high-purity Ar (99.9 %). The DSC measurement uncertainty is approximately ±2 K. The glass transition temperature (Tg), crystallization onset temperature (T_x), melting temperature (T_m), and liquidus

temperature (T_l) were determined using the two-tangents method.

Electrochemical impedance spectroscopy (EIS) was carried out utilizing a Biologic (SP-300) potentiostat/galvanostat over the frequency range of 100 kHz to 100 mHz with a 10 mV amplitude. Tests were performed in 0.9 wt% NaCl solution (pH 7.4 ± 0.1) at 37 °C following the ISO 10271 standard (for dentistry applications) using a conventional three-electrode setup. A 0.5 mm platinum wire and a NaCl-saturated Ag/AgCl served as the counter and reference electrode, respectively. Ribbon samples with an exposed area of 1 ± 0.1 cm^2, delimited by blocking varnish, were used as working electrodes. An open circuit potential (OCP) was recorded for 3600 s before each run to stabilize the interface. At least three measurements were acquired per alloy for reproducibility. Corrosion parameters were extracted using Power Suite software, and EIS fitting was performed in ZView (Scribner Associates Inc., Version 3.5b). Surface morphology and elemental analysis were characterized via scanning electron microscopy (SEM) at 10 kV using a TESCAN VEGA 3 microscope equipped with Energy-dispersive X-ray spectroscopy (EDX).

2.3. Microhardness measurements

The Vickers hardness of the melt-spun ribbons was determined using a microhardness tester (Zwick/Roell, EMCOTEST DURASCAN) with a 50 gf load and a 10 s hold time. The reported hardness value is the average of five independent measurements. Before conducting the Vickers hardness tests, the ribbons were sectioned and mounted in epoxy for cross-sectional analysis. The samples were ground stepwise with SiC papers to 4000 grit and then polished with a 1 μm diamond suspension to produce a mirror-like surface. A final polishing step with colloidal silica was applied to reduce surface deformation. The samples were then ultrasonically cleaned in ethanol and dried before the measurements. Indentations were made on the polished cross-sectional surface, and their dimensions were measured using a TESCAN MAGNA SEM. The SEM's built-in analysis software was used to determine the indent sizes and corresponding hardness values directly, ensuring accurate adjustment of the indent diagonal length. To prevent interference between indentations, they were spaced at least three times the diagonal length of each indent.

2.4. Cytocompatibility and inflammatory response

2.4.1. Cell culture conditions

Human bone marrow-derived mesenchymal stromal cells (hBMSCs, PCS-500-012) and human gingival fibroblasts (HGFs, CRL-2014) were cultured from the American Type Culture Collection (ATCC). hBMSCs were maintained in low-glucose DMEM (Merck, Milan, Italy) supplemented with 15 % fetal bovine serum (FBS) and 1 % penicillin/streptomycin (Merck, Milan, Italy). HGFs were cultured in αMEM (Merck, Milan, Italy) supplemented with 10 % FBS and 1 % penicillin/streptomycin. All cells were incubated at 37 °C, 95 % relative humidity, and 5 % CO_2. When cells reached 80–90 % confluence, they were detached using trypsin-EDTA (Merck, Milan, Italy), harvested, and used for experiments.

2.4.2. Indirect cytocompatibility assay

An indirect cytotoxicity test was conducted following ISO 10993 parts 5 and 12 guidelines to assess the potential cytotoxic effects of particles released from the ribbons. Briefly, the samples were immersed in an appropriate volume of FBS-free cell culture medium in accordance with ISO 10993-12 extraction ratio guidelines and placed on a shaker at 37 °C for 1, 3, and 7 days. Subsequently, the conditioned medium was collected, supplemented with 15 % FBS, and used for the assay. A total of 1.5×10^4 cells were seeded into a sterile 24-well plate. After 24 h, to allow sufficient adhesion and spreading, the culture medium was removed and replaced with the conditioned medium. Cellular metabolic activity was illustrated using the Alamar Blue assay according to the manufacturer's instructions. Briefly, a solution of Alamar Blue (0.015 % in complete culture medium) was added to the cells, which were then incubated for 3 h at 37 °C in the dark. Fluorescent signals were measured with the Spark spectrophotometer using excitation/emission wavelengths of 530/590 nm. The cells' metabolic activity was expressed as Relative Fluorescent Units (RFU), and results were compared with those of cells cultured in complete culture medium (Poly). Cell viability was also assessed using the LIVE/DEAD™ Viability/Cytotoxicity Kit, which utilizes the ability of viable cells to convert the non-fluorescent molecule Calcein AM into the brightly fluorescent Calcein. Dead cells are stained red by Ethidium homodimer-1 (EthD-1). Briefly, the culture medium was removed, and following a PBS wash, a solution containing Live/Dead reagents (2 μM Calcein AM and 4 μM EthD-1 in FluoroBrite™ DMEM) was added for 20 min. The cells were then observed using the EVOS FLoid Imaging System (ThermoFisher). Finally, the internalization and accumulation of the metal particles were confirmed using May-Grunwald/Giemsa staining.

2.4.3. Inflammatory response evaluation

To assess the inflammatory effects of the MG ribbons, HGFs were chosen for their relevance to inflammation and early tissue response [37]. In the experiment, 4×10^4 HGF cells per well were suspended in PureCol® EZ Gel solution (bovine type I collagen, 5 mg/mL, Merck, Milan, Italy) and placed in direct contact with the ribbon surfaces. The negative control group included the cell–collagen mixture without metal exposure. Cells were cultured for seven days, with 50 % of the growth medium replaced every two days to maintain nutrients and remove waste. No additional pro-inflammatory stimuli were introduced.

On day 7, cells were lysed with TRIzol™ (Thermo Fisher Scientific), and total RNA was isolated following the manufacturer's guidelines. RNA quantity and purity were measured with a NanoDrop™ OneC spectrophotometer. Subsequently, 0.5 μg of RNA was converted to cDNA using the Verso cDNA Synthesis Kit (Thermo Fisher Scientific) according to the recommended protocol.

Quantitative PCR (RT-qPCR) was conducted using SsoAdvanced™ Universal SYBR® Green Supermix (Bio-Rad Laboratories, Inc.) to measure the expression levels of angiogenic and inflammatory markers, including VEGF, COX2, and PTGES2. Reactions were performed on the CFX96 Touch™ Real-Time PCR Detection System (Bio-Rad Laboratories, Inc.). Expression values were normalized to the housekeeping gene ACTB (β-actin) and analyzed using the ΔΔCt method relative to the control group. Primer sequences are listed in the Supplementary Information (Table S1).

2.5. Statistical analysis

Biological assays were performed in triplicate. Data distribution was verified using the Shapiro-Wilk test. Multiple group comparisons were analyzed by one-way ANOVA, followed by Tukey's or Dunnett's post hoc test as appropriate for the inflammatory response analysis.

3. Results and discussion

3.1. Glass-forming ability (GFA) by calculating P_{HS} and P_{HSS}

High GFA in alloys is essential for obtaining bulk amorphous samples under relatively low quenching rates [38]. Various parameters are used to assess the overall GFA of alloys, including the supercooled region ($\Delta T_x = T_x - T_g$), the normalized glass transition temperature ($T_{rg} = T_g/T_l$) [39], and $\gamma = [T_x/(T_l + T_g)]$ [40,41]. To better predict the specific glass-forming composition (GFC), Inoue proposed using P_{HS} and P_{HSS} thermodynamic parameters in quaternary, quinary, and higher-order systems [42]. The current study adopts a thermodynamic approach to evaluate Inoue's criteria, which help explain GFA trends and guide alloy design by leveraging these thermodynamic parameters [42]. To ensure precise GFA assessment, the thermodynamic results were cross-

validated against conventional experimental indicators, such as T_{rg} and γ, as well as DSC and XRD measurements. According to Mansoori et al. [43], the P_{HS} parameter expresses the joint contribution of chemical mixing enthalpy (ΔH^C) and the mismatch entropy term ($\Delta S_\sigma/k_B$) adjusted by Boltzmann's constant (k_B). P_{HSS} further incorporates the configurational entropy ($\Delta S_{config}/R$) to account for the influence of increasing compositional complexity on GFA [29]. P_{HSS} has been used to predict the GFA of high-entropy alloys, calculated as follows:

$$P_{HS} = \Delta H^C(\Delta S_\sigma/k_B) \tag{1}$$

$$P_{HSS} = \Delta H^C(\Delta S_\sigma/k_B)(\Delta S_C/R) \tag{2}$$

In this context, ΔH^C refers to $\Delta S_\sigma/k_B$, and $\Delta S_C/R$, where R (= 8.314 J/K·mol) is the universal gas constant. More negative P_{HS} and P_{HSS} values are generally associated with improved GFA in the studied alloys. The chemical mixing enthalpy for multi-component alloy based on Miedema's model for amorphous systems [44,45] is given by:

$$\Delta H^C = \sum_{\substack{i=1 \\ i\neq j}}^{n} \sum_{j=1}^{n} \Delta H^C_{ij} \tag{3}$$

In this context, $\Delta H^C_{(i,j)}$ as given in Eqs. (4)–(7) [46] represents the impact of the binary interaction of constituent elements in the molten state (Table 1).

$$\Delta H^C_{I,J} = X_I X_J \left[f^I_J \Delta H^{int}_{IintJ} + f^J_I \Delta H^{int}_{JintI}\right] \tag{4}$$

$$\Delta H^{int}_{IinJ} = \frac{V_I^{2/3}}{\left(n_{ws}^{-1/3}\right)_{av}} \left\{ -P(\Delta\Phi^*)^2 + Q(\Delta n_{ws}^{1/3})^2 - R^* \right\} \tag{5}$$

$$f^I_J = X^S_J \left[1 + \gamma(X^S_I X^{S2}_J)\right] \tag{6}$$

$$X^S_I = \frac{X_I X_I^{2/3}}{X_I V_I^{2/3} + X_I V_B^{2/3}} \tag{7}$$

X, V, n_{ws}, and Φ^* denote the atomic fraction, molar volume, electron density, and work function of the alloying elements, respectively. The constants P, Q*, and R* represent element-specific parameters. For transition metal-non-transition metal alloy pairs, R^* is evaluated based on the extent of Brillouin-zone filling associated with the corresponding crystal structure. Except for Ti, all elements examined in this study exhibit negative chemical mixing enthalpies when substituted into Zr. The lowest ΔH^C value (−130.117 kJ/mol) was found for the Zr-Pt system. Adding Pd and Au elements results in attractive interactions with the main element Zr, with mixing enthalpies of −118.888 and −97.185 kJ/mol, respectively. The mixing enthalpy among the constituent elements directly governs the strength of atomic interactions. In general, a significant absolute value of the mixing enthalpy tends to suppress atomic diffusion and promote glass formation. Previous studies have suggested that $\delta \geq 6$ and $\Delta H^{mix} \leq -25$ kJ/mol favor the formation of amorphous structures [48].

The second parameter in the P_{Hs} and P_{HSS} formulation is the $\Delta S_\sigma/k_B$, which depends on atomic radii and increases with greater atomic-size disparity among the constituents. Following the approach of Mansoori et al., the mismatch entropy was determined through

$$\Delta S_\sigma = k_B \left[\frac{3}{2}(\zeta^2-1)y_1 + \frac{3}{2}(\zeta-1)^2 y_2 - \left\{\frac{1}{2}(\zeta-1)(\zeta-3) + ln\zeta\right\}(1-y_3)\right] \tag{8}$$

Here, k_B represents Boltzmann's constant, and ζ represents the atomic packing ratio, defined as $\frac{1}{1-\zeta}$ a thick random packing with a value of 0.64. y_1, y_2, and y_3 were evaluated using the relations given below, d_i and d_j denote the atomic diameters of i and j, respectively.

$$y_1 = \frac{1}{\sigma^3} \sum_{j>i=1}^{n} (d_i + d_j)(d_i - d_j)^2 x_i x_j \tag{9}$$

$$y_1 = \frac{\sigma^2}{(\sigma^3)^2} \sum_{j>i=1}^{n} (d_i + d_j)(d_i - d_j)^2 x_i x_j \tag{10}$$

$$y_3 = \frac{(\sigma^2)^3}{(\sigma^3)^2} \tag{11}$$

$$y_1 + y_2 + y_3 = 1 \tag{12}$$

$$\sigma^k = \sum\nolimits_{i=1}^{n} x_i d_i^k (k = 2, 3) \tag{13}$$

The last part of the P_{HSS} parameter relates to the $\Delta S_C/R$, as given in Eq. (14) [49]

$$\Delta S_c = -R \sum_{i=1}^{n} x_i Ln(x_i) \tag{14}$$

In this formulation, R denotes the universal gas constant, and x_i represents the elemental atomic fraction. Across the ZAFT-Cu alloy, $\Delta S_C/R$ increases with compositional complexity, independent of the added element. A large value of $\Delta S_C/R$ indicates a higher degree of configurational disorder, which is generally associated with improved GFA. ΔH^C, $\Delta S_\sigma/k_B$, $\Delta S_C/R$, P_{HS}, and P_{HSS} of the examined alloys were estimated using the Eqs. (1)–(4), summarized in Table 2.

P_{HSS} and P_{HS} were calculated as −6.50 and −6.38 (kJ/mol) for the ZAFT-Cu base alloy, and became more negative, reaching −10.21 and −9.91 (ZAFT-Pt), −10.61 and −10.30 (ZAFT-Pd), and −6.40 and −6.22 (ZAFT-Au). Binary mixing enthalpy values used in these calculations are provided as follows:

ΔH^{mix}_{Pd-Fe} = −5.40 kJ/mol; ΔH^{mix}_{Pd-Al} = −60.19 kJ/mol; ΔH^{mix}_{Pd-Ti} = −103.49 kJ/mol;
ΔH^{mix}_{Pt-Fe} = −16.79 kJ/mol; ΔH^{mix}_{Pt-Al} = −58.35 kJ/mol; ΔH^{mix}_{Pt-Ti} = −106.11 kJ/mol;

For the ZAFT-Au alloy, the P_{HSS} and P_{HS} parameters closely match those of the ZAFT-Cu alloy. This similarity arises from the relatively high mismatch entropy in the ZAFT-Cu alloys, despite the higher mixing entropy of ZAFT-Au. In the case of the ZAFT-Au alloy, Au and Fe exhibit a large positive enthalpy of mixing (ΔH^{mix}_{Au-Fe} = 10.37 kJ/mol), indicating a repulsive interaction that may reduce local structural compatibility. Meanwhile, all other constituent elements interact attractively in the liquid (ΔH^{mix}_{Au-Al} = −28.56 kJ/mol; ΔH^{mix}_{Au-Ti} = −71.93 kJ/mol).

While optimizing the GFA is essential, it is also important to evaluate how alloying elements influence biocompatibility to ensure that improvements in GFA do not compromise biological safety. The ZAFT-Pd alloy exhibits significantly more negative P_{HSS} and P_{HS} (at least 1.5

Table 1
Calculated mixing enthalpy values for the substitution of individual alloying elements into the Zr matrix, obtained using Miedema's model [43,47].

Element	Zr–Pt	Zr–Pd	Zr–Au	Zr–Cu	Zr–Fe	Zr–Al	Zr–Ti
ΔH^c (kJ/mol)	−130.117	−118.888	−97.185	−36.844	−31.238	−57.977	−0.080

Table 2
Values of ΔH^C, $\Delta S_\sigma/k_B$, $\Delta S_C/R$, P_{HS}, and P_{HSS} for the investigated components, derived from Eqs. (1)–(4).

Alloy	ΔH^C (kJ/mol)	$\Delta S_\sigma/k_B$	$\Delta S_C/R$	P_{HSS}	P_{HS}	Reference
$Zr_{62.5}Al_{10}Cu_{22.5}Fe_5$	−40.01	0.18	1.01	−7.27	−7.20	[13]
$Zr_{66.5}Cu_{16.5}Al_{10}Fe_5Ti_2$	−39.85	0.16	1.03	−6.50	−6.38	Base alloy
$Zr_{66.5}Pd_{16.5}Al_{10}Fe_5Ti_2$	−93.67	0.11	1.03	−10.61	−10.30	
$Zr_{66.5}Pt_{16.5}Al_{10}Fe_5Ti_2$	−99.09	0.10	1.03	−10.21	−9.91	
$Zr_{66.5}Au_{16.5}Al_{10}Fe_5Ti_2$	−73.99	0.084	1.03	−6.40	−6.22	

times) than the base alloy, indicating better GFA for the substituted composition. Additionally, the lowest mixing enthalpy (–99.09) was observed for the ZAFT-Pt alloy, in agreement with the binary Zr-Pt values (Table 1).

3.2. Structural and thermal investigations

Fig. 1(a) presents the XRD patterns recorded from the wheel and air side of the as-spun ribbons, all displaying a broad diffraction hump within the $38^\circ \leq 2\theta \leq 50^\circ$ range, confirming the amorphous structures. As shown in Fig. 1(b), the diffraction maxima shift to lower q values ($q = 4\pi \sin(\theta)/\lambda$, where λ is the X-ray wavelength) after adding Pd, Pt, and Au, indicating an increase in the average atomic spacing in the first coordination shell [50,51]. This trend reflects the replacement of smaller Cu atoms (0.128 nm) with larger Pd (0.137 nm), Pt (0.139 nm), and Au (0.144 nm), which leads to peak broadening and structural variations in short- and medium-range atomic ordering. Notably, ZAFT-Pd exhibits the highest packing density among the substituted alloys (q = 30.01 nm^{-1}), consistent with its highly negative P_{HSS} and P_{HS} values (−10.61 and −10.30), while ZAFT-Pt (29.81 nm^{-1}) shows a slightly lower packing density. The larger atomic size mismatch in Zr-Pd ($|r_{Pd} - r_{Zr}|/r_{Zr}$) = 0.145, compared to ($|r_{Pt} - r_{Zr}|/r_{Zr}$) = 0.132, and ($|r_{Au} - r_{Zr}|/r_{Zr}$) = 0.101 further enhances packing frustration, a mechanism known to improve GFA by suppressing atomic diffusion and crystallization

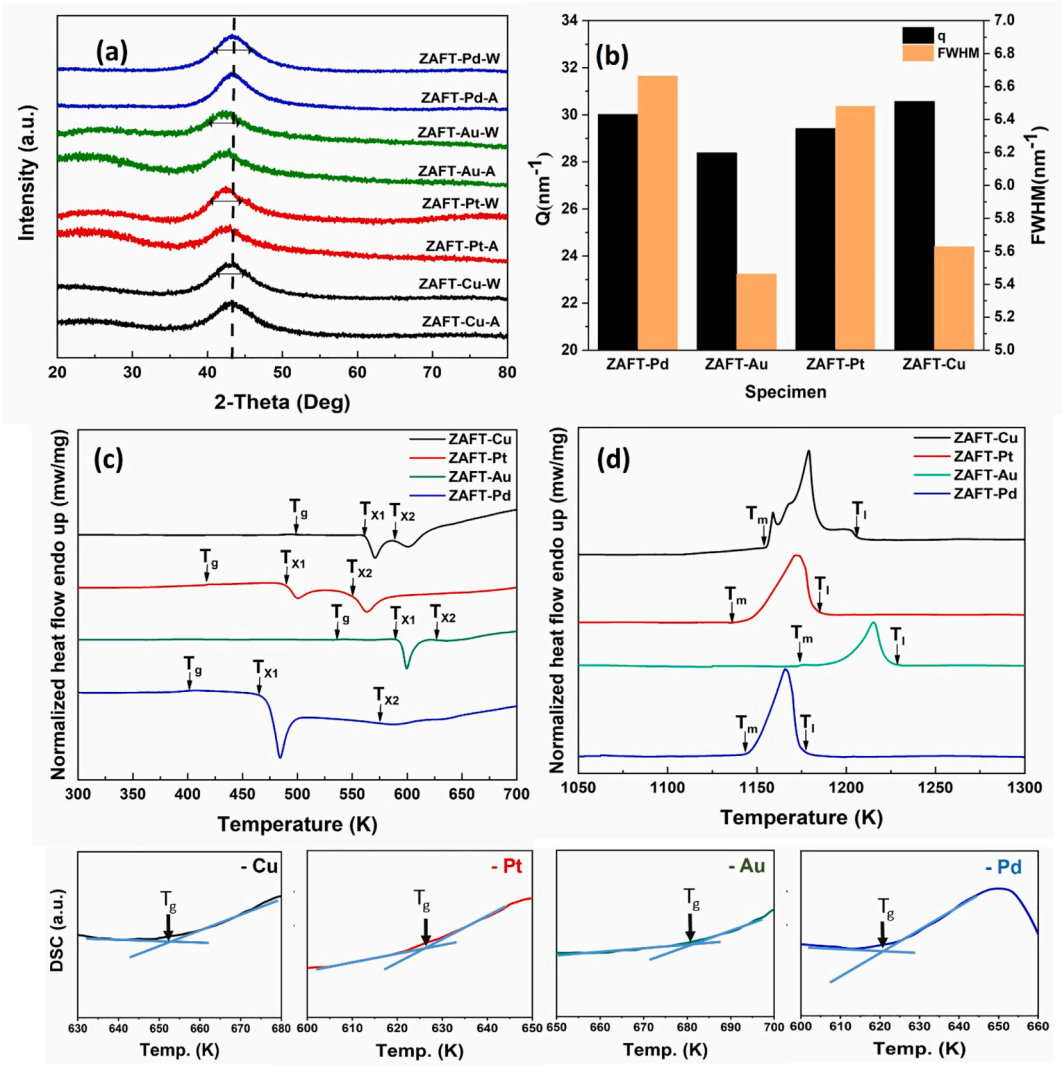

Fig. 1. (a) XRD patterns from the wheel (W) and air (A) sides of the as-spun ribbons. (b) q-position of the first broad diffraction maximum and corresponding FWHM (Δq) extracted from the wheel-side XRD profiles using Gaussian nonlinear fitting after background subtraction. (c) Melt-spun ribbon's high-temperature DSC scans conducted at 20 K/min heating rate, revealing the glass transition and crystallization behavior. Additional DSC plots at the bottom provide enlarged views of the T_g region for each alloy, and (d) the Melting event of the investigated alloys.

[43,52]. ZAFT-Pt (q = 29.81 nm^{-1}) appears to be the second densest alloy. In contrast, ZAFT-Au shows the lowest packing density (28.72 nm^{-1}), which can be attributed to the positive mixing enthalpy of the Au-Fe (ΔH^{mix}_{Au-Fe} = 10.37 kJ/mol), reducing local chemical affinity and weakening short-range structural cohesion [27]. Additionally, the Zr-Au pair exhibits a relatively minor size mismatch compared to Zr-Pd, contributing to reduced atomic packing frustration in ZAFT-Au.

Li et al. [53] reported a pronounced relationship between the full width at half maximum (Δq) of the first diffuse diffraction peak and GFA in a ternary alloy. They demonstrated that larger Δq values, which indicate broader diffraction maxima, are associated with higher GFA, while smaller Δq values correspond to reduced GFA. This relationship shows that broader peaks reflect greater topological disorder and enhanced packing frustration, both of which decrease atomic mobility and crystallization, thereby improving GFA [54]. For example, their Δq-based analysis enabled the identification of new BMG compositions such as $Zr_{43}Cu_{50}Cr_7$ and $Ir_{20}Co_{40}Ta_{40}$ [53], as well as the prediction of larger critical casting diameters (D_c) in the Zr-Cu-Al system. The Δq values were derived from the XRD patterns through nonlinear Voigt fitting of the first diffuse maximum. As shown in Fig. 1(b), ZAFT-Pd (6.663 nm^{-1}) and ZAFT-Pt (6.482 nm^{-1}) display larger Δq values, aligning with their superior GFA compared to other alloys. This indicates that Pd- and Pt-containing alloys are more readily vitrified during melt-spinning, producing amorphous ribbons with greater stability. These observations emphasize the crucial role of Pd in stabilizing the amorphous structure by increasing packing frustration and reducing atomic diffusivity [55].

This is evident in ZAFT-Pd, which not only shows the most negative P_{HSS} and P_{HS} values but also exhibits slightly higher structural disorder than ZAFT-Pt, supporting its superior GFA. Pd is also more effective than Pt in lowering the liquidus temperature (T_l) of Zr alloys, as seen in their eutectic points (1178 K for Zr-Pd vs. 1192 K for Zr-Pt). Additionally, Zr-Pd has a larger atomic size mismatch than Zr-Pt, which increases topological frustration and hinders atomic rearrangements. Consistently, ZAFT-Pd, with the highest GFA, also has a slightly larger Δq value than ZAFT-Pt, confirming its greater degree of disorder. In contrast, ZAFT-Au (5.462 nm^{-1}) shows lower packing density, aligning with its smaller P_{HSS} and P_{HS} values, which reduce the thermodynamic driving force for glass formation. Furthermore, Au has the smallest atomic radius mismatch with Zr, minimizing packing frustration and consequently limiting its GFA [56].

Fig. 1(c and d) display the representative DSC curves of the as-spun ribbons. These curves reveal the glass transition temperature (T_g), the onset of crystallization (T_x), and the melting behavior of the glassy alloys. The main thermal properties, including the size of the supercooled liquid region (SCLR) or ΔT_x ($\Delta T_x = T_{x1} - T_g$), as well as T_g, T_{x1}, T_{x2}, the onset melting temperature (T_m), and the liquidus temperature (T_l), are summarized in Table 3. The D_c values were estimated from DSC data of melt-spun ribbons using the empirical approach proposed by Liao et al. [57], and are commonly used as indirect indicators of GFA (Table 3).

Although the Au-containing alloy has a slightly higher reduced T_{rg} (0.556) than the Pd- and Pt-containing counterparts (0.527 and 0.525, respectively), T_{rg} alone cannot reliably differentiate GFA in multicomponent MGs. A multi-parameter assessment that combines kinetic indicators, ΔTx, and γ with a structural metric (Δq) provides a more accurate prediction of vitrification propensity. In the present alloys, ΔT_x = 75 K (Zr–Pt), 66 K (Zr–Pd), 62 K (Zr–Cu), and 50 K (Zr–Au), while γ = 0.386 (Zr–Pt), 0.383 (Zr–Pd), 0.382 (Zr–Cu), and 0.380 (Zr–Au). Consistently, Δq = 6.663 nm^{-1} (Zr–Pd), 6.482 nm^{-1} (Zr–Pt), and 5.462 nm^{-1} (Zr–Au), supporting the presence of greater packing frustration and thus enhanced GFA in the Pd- and Pt-containing alloys. The thermal behavior of the ZAFT-Cu alloy is similar to that of $Zr_{63}Cu_{20}Al_{10}Fe_5Ti_2$ reported by Qiang et al. [15], with slight differences in the T_g and T_{x1} attributed to variations in Cu content. The width of the ΔT_x serves as a key measure of kinetic stability; a broader ΔT_x suggests reduced atomic mobility and delayed crystallization, consistent with higher GFA [56].

Replacing Cu with Pd decreases T_g from 653 ± 2 K to 621 ± 2 K. The ZAFT-Pd alloy exhibits a lower T_{x1} (685 ± 2 K), which is likely linked to the lower T_l of Zr–Pd system (1178 K) compared with that of Zr-Cu [34]. Similarly, substituting Cu with Pt decreases T_g (653–627 ± 2 K) and T_{x1} (712–702 ± 2 K). However, ZAFT-Pt exhibits the widest SCLR, which may be attributed to the higher eutectic temperature of Zr-Pt (1192 K) relative to Zr-Pd [59]. In contrast, replacing Cu with Au raises T_g to 681 ± 2 K and T_{x1} of 725 ± 2 K, but results in the narrowest SCLR among the alloys. This weaker GFA is consistent with the absence of deep eutectic features in the Zr-Au phase diagram [60], which raises T_l to 1225 K. Therefore, Pd and Pt substitutions reduce T_g, extend ΔT_x, and enhance the kinetic stability of the glassy state. Conversely, Au increases T_g but narrows ΔT_x due to its unfavorable thermodynamics with Zr, emphasizing the combined influence of eutectic interactions and atomic size mismatch in governing GFA [56].

The T_{rg} values (0.55–0.59) for the substituted alloys remain within the typical range for Zr-based MGs, indicating competitive GFA [46,49]. Similarly, the γ value (0.38–0.383) falls within the standard range for MGs (0.35–0.50) [61], further supporting favorable GFA in the Pt-, Pd-, containing alloys relative to the Au-containing system. The simultaneous increase in T_{rg} and γ for the Pd- and Pt-containing compositions reflects both thermodynamic stabilization (lower crystallization driving force) and reduced atomic mobility, offering a mechanistic explanation for their superior GFA compared with the Au-containing alloy [42].

To validate the structural findings, as-spun ribbons of all four alloys, ZAFT-Cu, Pd, Pt, and Au, were examined using the HRTEM. Fig. 2(a–d) shows the HRTEM together with the corresponding SAED patterns. All HRTEM images exhibit uniform contrast without discernible lattice fringes, confirming the absence of long-range structural order. The disordered nature is further supported by the SAED patterns, which display broad diffuse halos characteristic of amorphous materials. These results indicate that all alloys retain a fully amorphous structure, consistent with the XRD analysis. The combination of diffuse SAED features and featureless HRTEM contrast corroborates the high degree of topological disorder linked to enhanced GFA [27].

3.3. Microhardness measurements

Table 4 presents a summary of the Vickers hardness (H_V) of the investigated melt-spun ribbons together with the corresponding estimated compressive yield strengths. The hardness and strength depend

Table 3
Thermal parameters of the investigated MG ribbons.

Alloys	T_g (K) (±2 K)	T_{x1} (K) (±2 K)	T_{x2} (K) (±2 K)	ΔT_x(K) (±2 K)	T_m (±2 K)	T_l	$T_{rg} = T_g/T_l$	$\gamma = T_x/(T_g + T_l)$	D_c (mm)
$Zr_{66.5}Cu_{16.5}Al_{10}Fe_5Ti_2$	653	712	738	62	1155	1209	0.541	0.382	3
$Zr_{66.5}Pd_{16.5}Al_{10}Fe_5Ti_2$	621	685	799	66	1141	1178	0.527	0.383	6
$Zr_{66.5}Pt_{16.5}Al_{10}Fe_5Ti_2$	627	702	763	75	1138	1192	0.525	0.386	7
$Zr_{66.5}Au_{16.5}Al_{10}Fe_5Ti_2$	681	725	769	50	1176	1225	0.556	0.380	2
$Zr_{60}Cu_{25}Al_{10}Fe_5$ [13]	655	767	–	112	–	1175	0.56	0.419	20
$Zr_{62}Cu_{21}Al_{10}Fe_5Ti_2$ [58]	662	740	–	78	1108	1185	0.559	–	–
$Zr_{63}Cu_{20}Al_{10}Fe_5Ti_2$ [17]	650	723	–	73	–	1206	–	0.401	–
$Zr_{65}Pd_{12.5}Ag_5Fe_{10}Al_{7.5}$ [34]	647	739	820	92	1151	1204	0.537	0.399	–

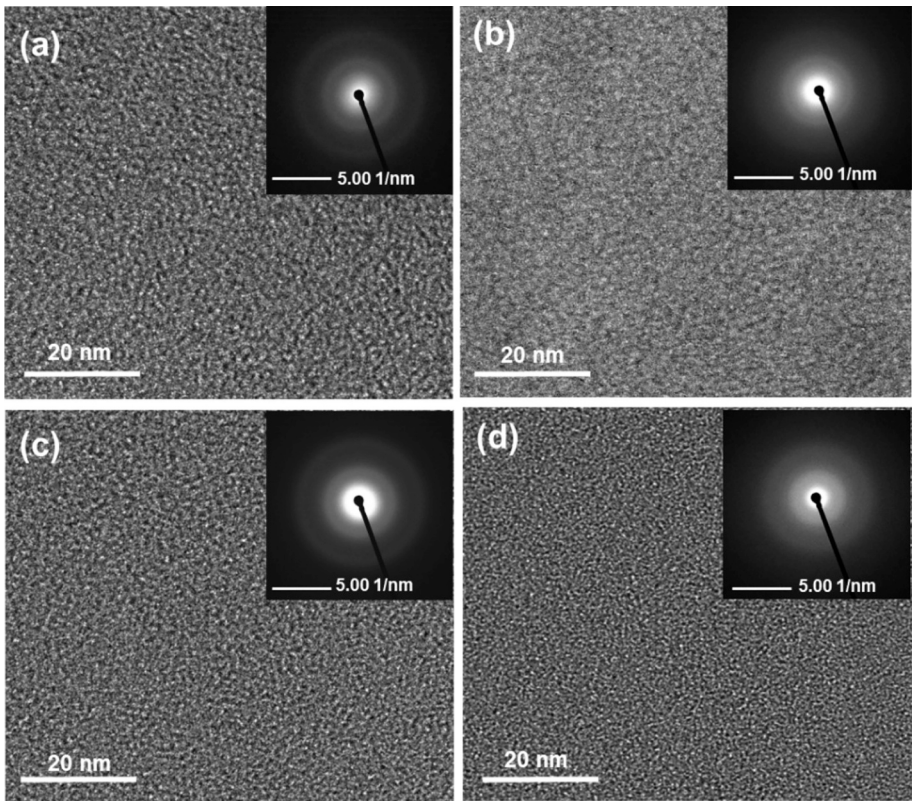

Fig. 2. HRTEM micrographs and corresponding SAED patterns (insets) of the amorphous ribbons: (a) ZAFT–Pd, (b) ZAFT–Pt, (c) ZAFT–Cu, and (d) ZAFT–Au.

Table 4
Microhardness and calculated compressive yield strength of the as-spun amorphous ribbons.

Alloys	Hardness (HV)	σ_y(MPa)
$Zr_{66.5}Cu_{16.5}Al_{10}Fe_5Ti_2$	590 ± 5	1927 ± 26
$Zr_{66.5}Pd_{16.5}Al_{10}Fe_5Ti_2$	654 ± 9	2136 ± 32
$Zr_{66.5}Pt_{16.5}Al_{10}Fe_5Ti_2$	683 ± 9	2231 ± 43
$Zr_{66.5}Au_{16.5}Al_{10}Fe_5Ti_2$	512 ± 6	1672 ± 36
$Zr_{54.4}Cu_{25.6}Fe_8Al_{12}$ [13]	563	1960
$Zr_{60}Cu_{20}Nb_5Al_{10}Fe_5$ [26]	422	1378
$Zr_{63}Cu_{20}Al_{10}Fe_5Ti_2$ [19]	–	1905 ± 25

strongly on alloy composition, which is governed by the interatomic bond strength [62]. In amorphous alloys, the absence of crystalline defects enhances atomic bonding, and this bonding, primarily dictated by cohesive energy, influences both hardness and elastic modulus [42]. In the present study, only microhardness was directly measured, while compressive yield strength (σ_y) was indirectly estimated using Eq. (15) [63].

$$\sigma_y = \frac{H_v \times g_0}{3} (g_0 = 9.81 m/s^2) \quad (15)$$

According to this equation, the σ_y is directly proportional to the H_v, while g_0 is a constant. Thus, the elastic modulus is not explicitly included, but it remains qualitatively correlated with H_v through their mutual dependence on cohesive energy. Among the studied alloys, ZAFT-Pt shows the highest hardness, whereas ZAFT-Au displays the lowest. The superior hardness of ZAFT-Pt correlates with its dense atomic structure, arising from the highly negative mixing enthalpy of Pt-Zr, Fe, Al, and Ti, which enhances atomic bond strength. In contrast, ZAFT-Pd exhibits lower hardness despite its highly negative P_{HHS} and P_{HS} values. This reduction may stem from the intrinsically lower hardness and bulk modulus of Pd relative to Pt, although both elements preferentially bond with Zr, Fe, and Al. The lowest hardness in ZAFT-Au likely results from the weak and unfavorable interactions of Au with the other constituents, which disrupts short-range order and may even induce localized segregation [27]. Fig. 3(a′–d′) displays SEM micrographs of the micro-indentation tests. The hardness values (Table 4) are consistent with those reported for other Zr-based MGs [17,59,60]. These trends emphasize that hardness in MGs is not solely dictated by global thermodynamic parameters (ΔH_{mix}, P_{HSS}) but also by the intrinsic mechanical properties of the participating elements and their ability to enhance short-range ordering, thereby linking atomic-scale interactions to macroscopic mechanical response [42]. This can be mechanistically understood in terms of atomic packing and bond strength. The highly negative enthalpy of mixing in Zr-Pt (−130 kJ/mol) and Zr-Pd (−118 kJ/mol) promotes dense atomic arrangements and strong short-range bonding, which directly translates into higher hardness and compressive strength. In contrast, the positive mixing enthalpy for Au-Fe (+10.37 kJ/mol) weakens local bonding and reduces structural cohesion, explaining the lower hardness observed in ZAFT-Au.

3.4. Corrosion performance

Fig. 4 shows the short-term electrochemical impedance spectroscopy (EIS) results after one-hour immersion of the MG ribbons in a NaCl solution. The EIS plots were fitted using the equivalent circuit model in Fig. 4a, with dashed lines representing the simulated curves. The equivalent circuit comprises the solution resistance (Rs) and the constant phase element (CPE), which replaces the ideal capacitance (C) to capture surface heterogeneities such as roughness and local porosity resulting from rapid solidification. These features produce non-ideal capacitive behavior [64]. The charge-transfer resistance (R_1) reflects resistance to electron transfer at the alloy-electrolyte interface; a higher R_1 corresponds to improved corrosion resistance due to the formation of a stable passive film. R_S denotes the electrolyte resistance between the working and reference electrodes and may vary with surface morphology or compositional differences that influence ion transport

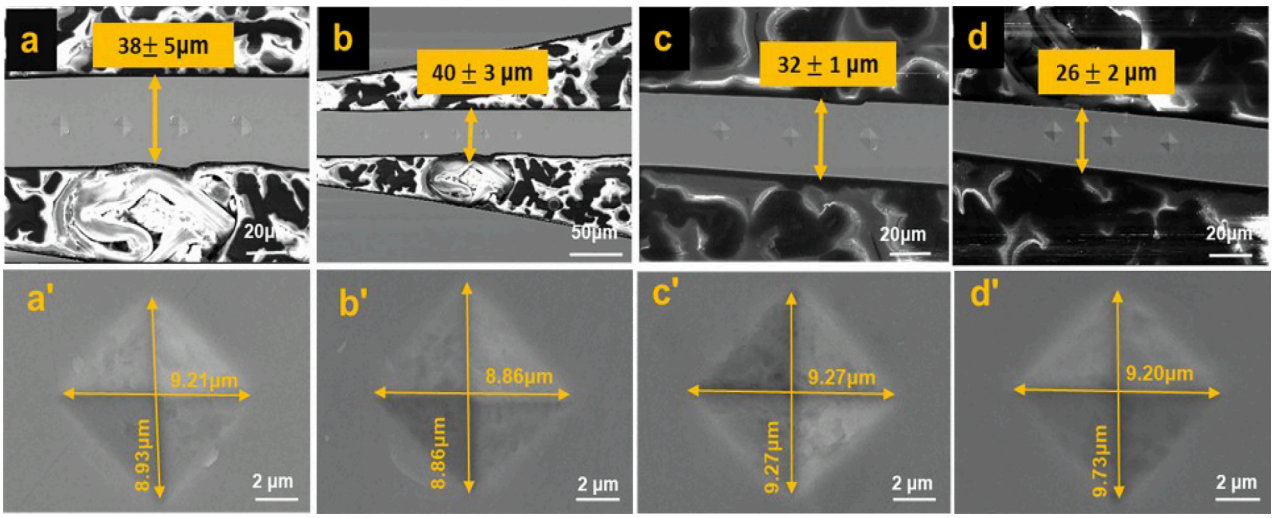

Fig. 3. Micro-indentation imprints on the cross-section of as-spun amorphous ribbons. (a, a') ZAFT-Pd, (b, b') ZAFT-Pt, (c, c') ZAFT-Cu, and (d, d') ZAFT-Au.

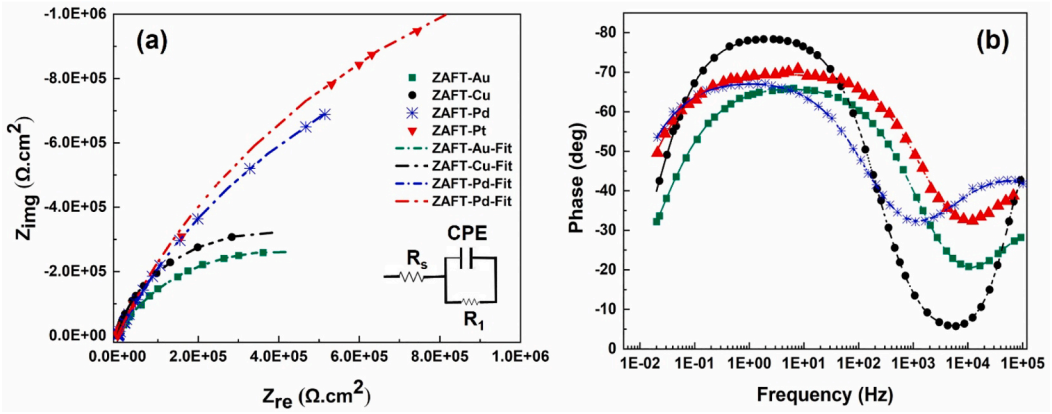

Fig. 4. (a) Nyquist and (b) Bode phase responses of the Zr-based MG ribbons in 0.9 wt% NaCl at 37 °C.

[65]. The Nyquist plots show incomplete semicircles, indicating effective barrier properties and robust surface passivation. Table 5 lists the best-fit parameters ($\chi^2 < 0.003$) obtained from the equivalent circuit. The double-layer-related CPE exponent (n) exceeds 0.9 [66]. Among the alloys, ZAFT-Pt shows the largest capacitive loops, reflecting superior barrier properties and stronger metal-electron interactions, consistent with its superior corrosion resistance. The improved electron–ion interactions in Pt- and Pd-containing surfaces likely facilitate the formation of thicker and more stable passive oxide layers [27]. Consistently, the Bode–phase plots of ZAFT-Pt display a distinct low-frequency hump (~10 Hz) with a high phase angle (~70°), surpassing that of the other alloys.

Table 5 shows that ZAFT-Pt and ZAFT-Pd have the highest Rs values. The Rs ranges from 11.52 ± 0.17 to 34.30 ± 0.82, but exerts minimal influence on the overall electrochemical trends. The CPE exponent n remains >0.9, confirming the reliability of the fits. Slightly higher CPE values for Pt- and Pd-containing alloys indicate a more capacitive interface, which is typically associated with enhanced charge storage behavior and improved passivation, contributing to lower R_1. The corrosion resistance of Zr-based metallic glasses mainly arises from the development of stable passive surface layers [67].

Ion-electron interactions at the alloy-electrolyte interface are governed by ZrO_2, TiO_2, and PdO surface oxide [68,69]. EDS analysis (Table 6) confirmed the presence of these oxide-forming elements (Zr, Ti, Pd) on the alloy surfaces after EIS testing. The excellent corrosion

Table 5
Equivalent circuit parameters obtained after 1 h immersion in 0.9 wt% NaCl solution.

Alloys	R_s ($\Omega\cdot cm^2$)	CPE ($\mu F\cdot cm^{-2}.Sn^{-1}$)	n	R_1 ($k\Omega\cdot cm^2$)	χ^2
$Zr_{66.5}Cu_{16.5}Al_{10}Fe_5Ti_2$	26.52 ± 0.19	6.53 ± 0.12	0.917 ± 0.007	542 ± 10	1.0×10^{-4}
$Zr_{66.5}Pd_{16.5}Al_{10}Fe_5Ti_2$	16.07 ± 0.11	4.92 ± 0.03	0.960 ± 0.004	556 ± 11	1.3×10^{-3}
$Zr_{66.5}Pt_{16.5}Al_{10}Fe_5Ti_2$	11.52 ± 0.17	3.12 ± 0.08	0.931 ± 0.001	623 ± 56	0.3×10^{-4}
$Zr_{66.5}Au_{16.5}Al_{10}Fe_5Ti_2$	34.30 ± 0.82	7.27 ± 0.26	0.906 ± 0.004	408 ± 34	2.1×10^{-4}

Table 6
EDX results acquired from the indicated spots in Fig. 5(c) and (d).

Element (%at) Spots	Zr	Al	Fe	Ti	Cu	Au	O
1	64.40	7.26	4.81	1.72	14.43	–	7.38
2	20.34	4.47	3.11	0.83	10.70	–	60.55
3	65.31	8.35	4.68	1.53	–	13.61	6.52
4	26.63	3.96	2.95	0.78	–	9.25	56.43

resistance of MGs results from factors such as chemical composition, structural and compositional uniformity, and their amorphous structure [70]. In particular, the absence of grain boundaries eliminates preferential corrosion sites, improving long-term stability [71]. Zhang et al. [72] emphasized the role of atomic mobility in amorphous alloys as a key factor influencing electrochemical behavior. They proposed that, unlike crystalline materials, MGs are inherently metastable and possess elevated atomic mobility due to their high-energy structural state, which promotes electrochemical activity and enables rapid formation of protective passivation layers [66].

Fig. 5 shows the post-EIS surface morphologies of the alloys. ZAFT-Pt and ZAFT-Pd surfaces appear free of large pits (Fig. 5a and b), confirming their strong corrosion resistance. By contrast, ZAFT-Au exhibits micro-scale pitting and inhomogeneous attack (Fig. 5d), while ZAFT-Cu shows moderate pitting (Fig. 5c). Although some minor damage was present, no severe degradation occurred, confirming good durability in NaCl solution (Fig. 5). Nevertheless, the Cu- and Au-containing alloys exhibited small cracks and pitting, indicating higher susceptibility to corrosion under the tested conditions.

Notably, the superior corrosion resistance of Pt- and Pd-containing MGs can be linked to their stronger chemical affinity with Zr and other constituents, which promotes the rapid formation of stable passive films. Conversely, the weaker interactions involving Au reduce film stability, leading to pitting corrosion. These findings highlight the connection between alloy chemistry, amorphous structure, and electrochemical passivation behavior [73,74]. Mechanistically, the passive films on ZAFT-Pd and ZAFT-Pt are enriched in ZrO_2 and TiO_2, further stabilized by PdO or PtO species. These oxides exhibit low solubility and high stability in chloride-containing environments, accounting for the high R_1 values observed in the EIS spectra. In contrast, ZAFT-Au suffers from weaker Au-Fe interactions, which limit protective oxide development and favor localized pitting, as confirmed by SEM after EIS testing.

3.5. Indirect cytocompatibility and inflammatory gene expression

Fig. 6 presents the indirect cytocompatibility results after 24 h of cell exposure to supernatants collected from ZAFT-Pd, ZAFT-Cu, ZAFT-Pt, or ZAFT-Au samples, immersed in FBS-free culture medium for 1, 3, and 7 days. The results indicate that the samples did not adversely affect the cells' metabolic activity. Samples incubated in culture medium for 1 and 3 days exhibit comparable performance, with no statistically significant differences observed.

The situation differs for samples immersed in the culture medium for 7 days. On the one hand, all samples are cytocompatible, as the metabolic activity of cells exposed to the eluates is comparable to or higher than that of cells cultivated in polystyrene wells. On the other hand, the ZAFT-Au, ZAFT-Pt, and ZAFT-Cu samples, but not ZAFT-Pd, enhanced cellular metabolic activity, with Zr-Au-Al-Fe-Ti eliciting a statistically

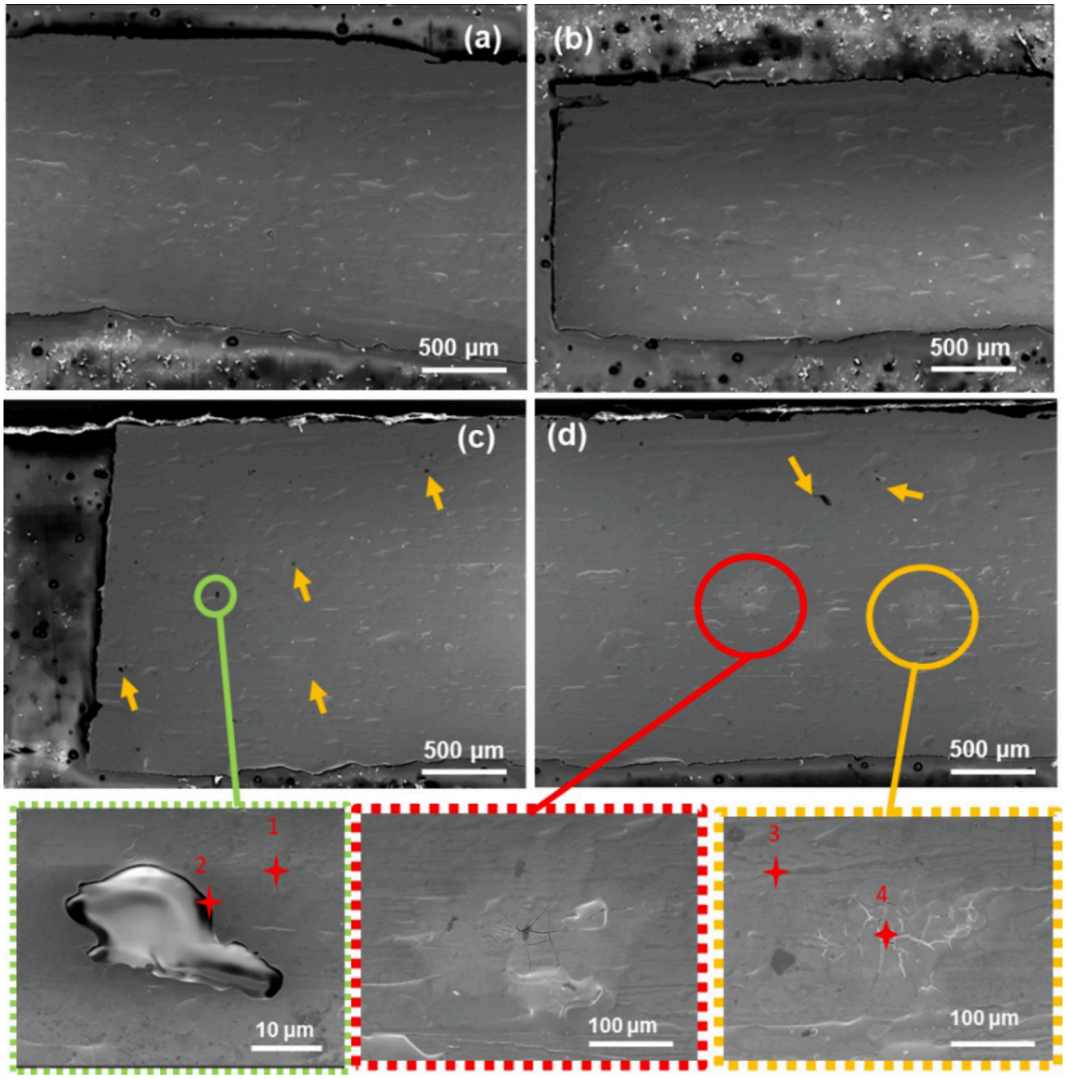

Fig. 5. SEM images of the amorphous ZAFT-Pd (a), ZAFT-Pt (b), ZAFT-Cu (c), and ZAFT-Au (d) ribbons following EIS testing.

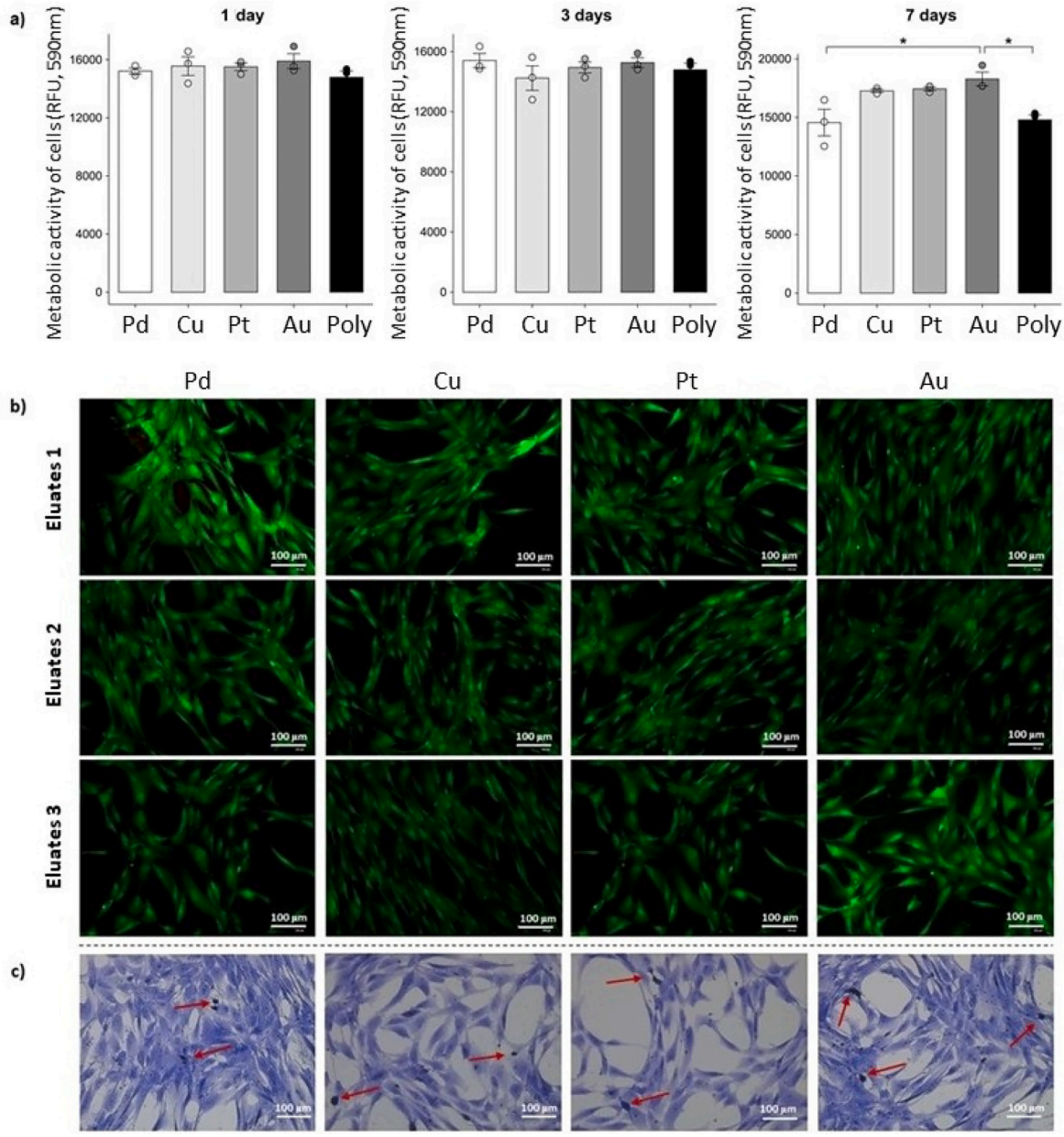

Fig. 6. Indirect cytocompatibility results after 24 h of cell exposure to the supernatant collected from the samples, which were immersed in FBS-free culture medium for 1, 3, and 7 days. (a) Metabolic activity results obtained using the Alamar Blue assay; (b) Live/Dead assay staining live cells in green and dead cells in red; (c) Metal particle internalization visualized with May-Grünwald/Giemsa staining (red arrows). *$p < 0.05$.

significant cellular response ($p < 0.05$). This enhanced response may be attributed to the higher corrosion rate of ZAFT-Au, which leads to greater ion release and may transiently stimulate metabolic activity in human mesenchymal stromal cells [75]. The steady response observed for ZAFT-Pd on cell activity aligns with the delayed stabilization of palladium observed in the corrosion results. Pd demonstrates excellent barrier properties as a result of stable and protective oxide layers formation. Interestingly, the ZAFT-Cu and ZAFT-Pt samples exhibit similar performance, suggesting that the level of copper ions released remains below cytotoxic thresholds. Overall, these findings highlight the link between corrosion behavior and cytocompatibility, as alloys exposed to simple immersion (without electrochemical stimulation) release ions in a manner distinct from active corrosion conditions. This underscores the importance of studying alloy behavior under physiological conditions to ensure biocompatibility in practical applications. The cytocompatibility of the samples is further supported by the Live/Dead assay results shown in Fig. 6b, revealed no detectable dead cells (red staining). As detailed in Section 2.4.2, the internalization and accumulation of metal particles were verified using May-Grünwald/Giemsa staining, with the results presented in Fig. 6c. The detection of metallic particles within the cells, including some accumulation, is evident; however, this did not compromise cell viability, further confirming the materials' cytocompatibility.

Overall, the superior performance of ZAFT-Au and the long-term stabilization of ZAFT-Pd position these alloys as promising candidates for biomedical use. Inflammation is a crucial process in initiating wound healing; however, when exacerbated, it can hinder tissue regeneration and contribute to chronic wound formation [9,76]. The material selected for implantation is a key factor in directing this response, as the release of metallic ions may positively or negatively influence the local cellular environment and the regenerative cascade. Extensive literature has attributed pro-inflammatory roles to Cu, Pt, and Pd [9,76] ions,

while Au [77] is generally recognized for its anti-inflammatory properties. To evaluate whether these trends hold in our MG system, we exposed human gingival fibroblasts (HGFs) to Zr-based MG ribbons in a collagen matrix, in the absence of exogenous inflammatory stimuli, and assessed gene expression after 7 days.

The expression of two inflammation-related markers, COX2 and PTGES2, and the angiogenesis mediator VEGF, was quantified using RT-qPCR. These markers are associated with the early inflammatory response; during acute inflammation, VEGF upregulation and activation of the COX2/PTGES2 axis promote immune cell recruitment and production of inflammatory mediators such as PGE_2 [78]. As depicted in Fig. 7(b and c), COX2 and PTGES2 expression in Zr-Cu and Zr-Pt was downregulated, following a similar trend to the Zr-Au group. Consistent with the downregulation of COX2/PTGES2, VEGF expression (Fig. 7d) remained at baseline for ZAFT-Cu, ZAFT-Pt, and ZAFT-Au, indicating the absence of a pro-inflammatory response. Since the COX2/PTGES2/PGE_2 pathway is predominantly activated in damaged tissues [78], our findings imply that Zr-based metallic glasses do not create a damage-associated inflammatory environment.

4. Conclusions

This study focused on the development and evaluation of Ni- and Cu-free Zr-based MGs intended for biomedical use. The investigated alloys $Zr_{66.5}Pd_{16.5}Al_{10}Fe_5Ti_2$, $Zr_{66.5}Pt_{16.5}Al_{10}Fe_5Ti_2$, and $Zr_{66.5}Au_{16.5}Al_{10}Fe_5Ti_2$ exhibit promising combinations of GFA, mechanical properties, corrosion performance, cytocompatibility, and immunological response. Based on these findings, the following conclusions are drawn:

Among the studied alloys, $Zr_{66.5}Pd_{16.5}Al_{10}Fe_5Ti_2$ and $Zr_{66.5}Pt_{16.5}Al_{10}Fe_5Ti_2$ ribbons exhibit enhanced GFA when assessed by ΔT_x, γ, Δq, *and* P_{HS}/P_{HSS}, together indicating their superior glass-forming behavior. Notably, $Zr_{66.5}Pt_{16.5}Al_{10}Fe_5Ti_2$ shows a slightly larger ΔT_x and estimated D_c, whereas $Zr_{66.5}Pd_{16.5}Al_{10}Fe_5Ti_2$ exhibits more negative P_{HS}/P_{HSS} and a marginally larger Δq, indicating comparable yet complementary advantages.

$Zr_{66.5}Pt_{16.5}Al_{10}Fe_5Ti_2$ exhibited the highest thermal stability and mechanical strength, reflected in its superior hardness and compressive yield strength, which stem from dense atomic packing. However, this mechanical advantage was accompanied by slightly reduced cytocompatibility compared with $Zr_{66.5}Au_{16.5}Al_{10}Fe_5Ti_2$, suggesting a potential trade-off between structural performance and biological response.

Electrochemical testing demonstrated excellent corrosion resistance for $Zr_{66.5}Pd_{16.5}Al_{10}Fe_5Ti_2$ and $Zr_{66.5}Pt_{16.5}Al_{10}Fe_5Ti_2$, attributable to the development of stable passive films. In contrast, $Zr_{66.5}Au_{16.5}Al_{10}Fe_5Ti_2$ exhibited reduced corrosion resistance, which may compromise its long-term durability in physiological environments.

All alloys supported cell viability and metabolic activity. RT-qPCR analysis revealed that $Zr_{66.5}Pt_{16.5}Al_{10}Fe_5Ti_2$, despite containing elements sometimes associated with pro-inflammatory behavior, did not upregulate COX2 or PTGES2. Its inflammatory gene expression was comparable to that of $Zr_{66.5}Au_{16.5}Al_{10}Fe_5Ti_2$. VEGF expression remained at baseline in all alloys except $Zr_{66.5}Pd_{16.5}Al_{10}Fe_5Ti_2$, which showed a modest 1.7-fold increase, suggesting a potential pro-angiogenic effect. These results indicate that the inflammatory response is not solely determined by elemental composition but also by corrosion resistance and ion-release kinetics, which are governed by the amorphous structure.

In conclusion, Ni- and Cu-free Zr-based MGs containing Pd, Pt, or Au offer promising combinations of mechanical strength, corrosion resistance, and biological compatibility. Integrating immunological assays into the evaluation framework emphasizes the importance of a broader and more systematic understanding of host-material interactions. These results support the advancement of Ni- and Cu-free Zr-based MGs for long-term biomedical use and highlight the importance of further in-vivo studies to confirm clinical feasibility. Future investigations should incorporate transcriptomic profiling and broader immunophenotyping to elucidate cellular pathways and provide deeper mechanistic insight into the pathways through which these materials modulate the inflammatory microenvironment.

CRediT authorship contribution statement

Fereshteh Sourani: Writing – original draft, Software, Resources, Methodology, Investigation, Funding acquisition, Formal analysis, Data curation, Conceptualization. **Parthiban Ramasamy:** Writing – review & editing, Visualization, Validation, Resources, Methodology, Investigation, Conceptualization. **Elham Sharifikolouei:** Writing – original draft,

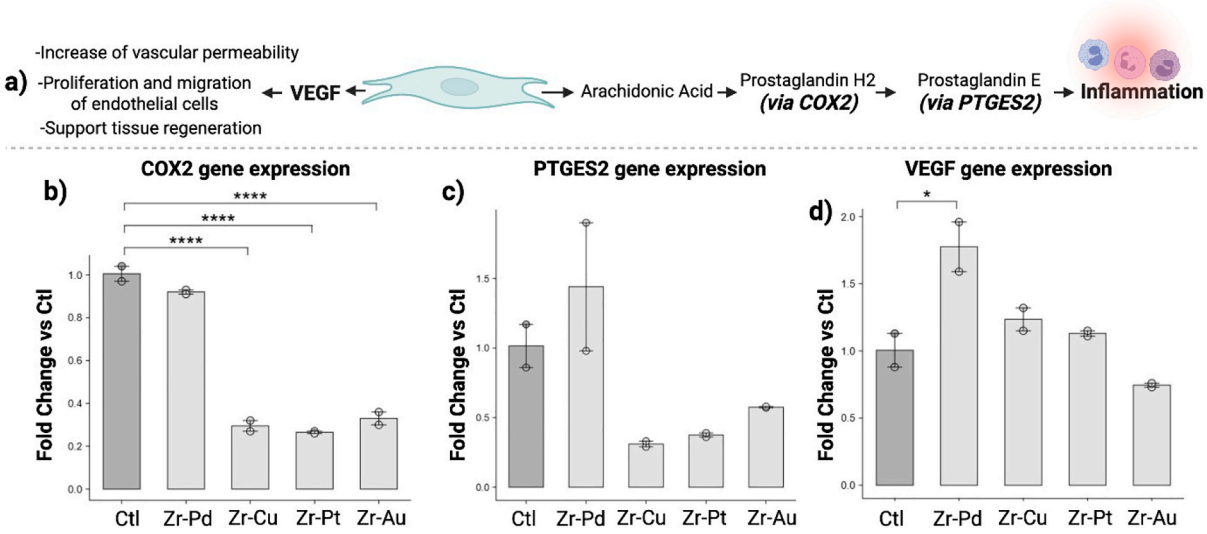

Fig. 7. Evaluation of COX-2, PTGES-2, and VEGF expression rate in human gingival fibroblast (HGF) after 7 days of exposure to Zr-based MG ribbons. (a) Schematic representation of the metabolic pathway involved in Prostaglandin E synthesis. Arachidonic acid is converted into prostaglandin H2 (PGH2) by COX2 and subsequently into prostaglandin E2 (PGE2) by PTGES2, leading to inflammatory activation. In parallel, HGF cells release VEGF, promoting vascular permeability and tissue regeneration. (b) COX2 gene expression is significantly downregulated in all groups compared to control (CTL), with the most potent suppression observed for Zr-Cu and Zr-Pt alloys (****$p < 0.0001$). (c) PTGES2 gene expression is moderately upregulated in the Zr-Pd group but reduced in Zr-Cu, Zr-Pt, and Zr-Au. (d) VEGF gene expression shows a 1.7-fold upregulation (*$p < 0.05$) in the Zr-Pd group, while the other groups show a basal level of expression.

Visualization, Validation, Methodology, Investigation, Formal analysis, Conceptualization. **Christoph Gammer:** Visualization, Validation, Resources, Methodology. **Alessandro Scalia:** Writing – original draft, Formal analysis. **Tiziana Brosio:** Writing – original draft, Formal analysis. **Andrea Cochis:** Writing – review & editing, Writing – original draft. **Lia Rimondini:** Writing – review & editing, Writing – original draft. **Jürgen Eckert:** Writing – review & editing, Visualization, Validation, Supervision, Resources, Project administration, Conceptualization.

Declaration of competing interest

The authors declare the following financial interests/personal relationships which may be considered as potential competing interests: The authors declare the following financial interests/personal relationships which may be considered as potential competing interests: Fereshteh Sourani reports financial support was provided by Austrian Science Fund (FWF). If there are other authors, they declare that they have no known competing financial interests or personal relationships that could have appeared to influence the work reported in this paper.

Acknowledgments

Fereshteh Sourani would like to thank the Austrian Science Fund (FWF) for the financial support under Grant DOI 10.55776/ESP453. The authors would also like to thank Eray Yüce for his support in preparing the ribbon samples. The authors also thank Dr. Lidija Rafailovic and Huanqing Zhang for providing access to the Biologic (SP-300) potentiostat/galvanostat.

Appendix A. Supplementary data

Supplementary data to this article can be found online at https://doi.org/10.1016/j.matdes.2025.115227.

Data availability

Data will be made available on request.

References

[1] Y. Prabhu, A.K. Srivastav, D.V. Gunderov, J. Bhatt, Thermodynamic model to predict bulk metallic glass forming composition in Zr–Cu–Fe–Al system and understanding the role of Dy addition, Physica B Condens. Matter. 624 (2022) 413416, https://doi.org/10.1016/j.physb.2021.413416.
[2] K. Zhou, Y. Liu, S. Pang, T. Zhang, Formation and properties of centimetre-size Zr–Ti–Cu–Al–Y bulk metallic glasses as potential biomaterials, J. Alloys Compd. 656 (2016) 389–394, https://doi.org/10.1016/j.jallcom.2015.09.254.
[3] Y. Luo, Y. Jiang, P. Zhang, X. Wang, H. Ke, P. Zhang, A novel Ni-Free Zr-based bulk metallic glass with high glass forming ability, corrosion resistance and thermal stability, Chin. J. Mech. Eng. 33 (2020) 68, https://doi.org/10.1186/s10033-020-00482-y.
[4] N. Ghodki, S. Jha, S.S. Alla, Y.C. Yang, G.M. Pharr, S. Mukherjee, Deformation behavior of thermally rejuvenated Zr–Cu–Al–(Ti) bulk metallic glass, Sci. Rep. 14 (2024) 71658, https://doi.org/10.1038/s41598-024-71658-y.
[5] Y. Liu, Y.M. Wang, H.F. Pang, Q. Zhao, L. Liu, A Ni-free ZrCuFeAlAg bulk metallic glass with potential for biomedical applications, Acta Biomater. 9 (6) (2013) 7043–7053, https://doi.org/10.1016/j.actbio.2013.02.019.
[6] L. Huang, D. Qiao, B.A. Green, P.K. Liaw, J. Wang, S. Pang, T. Zhang, Bio-corrosion study on zirconium-based bulk-metallic glasses, Intermetallics 17 (2009) 195–199, https://doi.org/10.1016/J.INTERMET.2008.07.020.
[7] N. Bin Hua, R. Li, J.F. Wang, T. Zhang, Biocompatible Zr–Al–Fe bulk metallic glasses with large plasticity, Sci. China Phys. Mech. Astron. 55 (2012) 1664–1669, https://doi.org/10.1007/s11433-012-4831-5.
[8] P. Chhay, M. Murphy-Marion, Y. Samson, D. Girard, Activation of human eosinophils with palladium nanoparticles (Pd NPs): importance of the actin cytoskeleton in Pd NPs-induced cellular adhesion, Environ. Toxicol. Pharmacol. 57 (2018) 95–103, https://doi.org/10.1016/J.ETAP.2017.12.002.
[9] A. Flemming, Copper boosts pro-inflammatory state of macrophages, Nat. Rev. Immunol. 23 (2023) 344, https://doi.org/10.1038/s41577-023-00889-3.
[10] C.J. Price, P.L. Strong, F.J. Murray, M.M. Goldberg, Developmental effects of boric acid in rats related to maternal blood Boron concentrations, Biol. Trace Elem. Res. 66 (1998) 359–375, https://doi.org/10.1007/BF02783148/METRICS.
[11] M.H. Abbasi, R. Tavakoli, S.G. Shabestari, A novel criterion for predicting the glass-forming ability in Zr-Cu-Al ternary alloys: a molecular dynamics study, Intermetallics 164 (2024) 108126, https://doi.org/10.1016/J.INTERMET.2023.108126.
[12] K. Jin, J.F. Löffler, Bulk metallic glass formation in Zr–Cu–Fe–Al alloys, Appl. Phys. Lett. 86 (2005) 1–3, https://doi.org/10.1063/1.1948513.
[13] Q.S. Zhang, W. Zhang, D.V. Louzguine-Luzgin, A. Inoue, High glass-forming ability and unusual deformation behavior of New Zr–Cu–Fe–Al bulk metallic glasses, Mater. Sci. Forum 654–656 (2010) 1042–1045, https://doi.org/10.4028/WWW.SCIENTIFIC.NET/MSF.654-656.1042.
[14] Y.J. Yang, B.Y. Cheng, Z.S. Jin, H.X. Gao, M.Z. Ma, X.Y. Zhang, Crystallization kinetics and mechanical properties of Zr56Cu24Al9Ni7–xTi4Agx (x = 0, 1, 3, 5, and 7) metallic glasses, J. Alloys Compd. 816 (2020) 152589, https://doi.org/10.1016/J.JALLCOM.2019.152589.
[15] Q.K. Jiang, X.D. Wang, X.P. Nie, G.Q. Zhang, H. Ma, H.-J. Fecht, J. Bendnarcik, H. Franz, Y.G. Liu, Q.P. Cao, J.Z. Jiang, Zr-(Cu,Ag)-Al bulk metallic glasses, Acta Mater. 56 (2008) 1785–1796, https://doi.org/10.1016/j.actamat.2007.12.030.
[16] G. Cao, K. Liu, G. Liu, H. Zong, H. Bala, B. Zhang, Improving the glass-forming ability and the plasticity of Zr–Cu–Al bulk metallic glass by addition of Nb, J. Non Cryst. Solids 513 (2019) 105–110, https://doi.org/10.1016/J.JNONCRYSOL.2019.03.009.
[17] J.B. Qiang, W. Zhang, G.Q. Xie, A. Inoue, Effect of Ti addition on the crystallization behavior and glass-forming ability of Zr–Al–Cu alloys, J. Non Cryst. Solids 354 (2008) 2054–2059, https://doi.org/10.1016/j.jnoncrysol.2007.11.002.
[18] K. Han, H. Jiang, Y. Wang, J. Qiang, C. Yu, Antimicrobial Zr-based bulk metallic glasses for surgical devices applications, J. Non Cryst. Solids 564 (2021) 120827, https://doi.org/10.1016/J.JNONCRYSOL.2021.120827.
[19] H. Shi, W. Zhao, X. Wei, Y. Ding, X. Shen, W. Liu, Effect of Ti addition on mechanical properties and corrosion resistance of Ni-free Zr-based bulk metallic glasses for potential biomedical applications, J. Alloys Compd. 815 (2020) 152636, https://doi.org/10.1016/j.jallcom.2019.152636.
[20] J.J. Oak, D.V. Louzguine-Luzgin, A. Inoue, Investigation of glass-forming ability, deformation and corrosion behavior of Ni-free Ti-based BMG alloys designed for application as dental implants, Mater. Sci. Eng. C 29 (2008) 322–327, https://doi.org/10.1016/j.msec.2008.07.009.
[21] Q. Wu, H. Ge, P. Zhang, N. Yu, A. Yan, Effects of Nb addition on glass-forming ability and magnetization behaviors of nanocomposite Nd–Fe–B–Nb strip flakes, Jpn. J. Appl. Phys. 53 (2014) 053001, https://doi.org/10.7567/JJAP.53.053001.
[22] Y. Li, W. Zhang, C. Dong, A. Inoue, Enhancement of glass-forming ability and corrosion resistance of Zr-based Zr–Ni–Al bulk metallic glasses with minor addition of Nb, J. Appl. Phys. 110 (2011) 023520, https://doi.org/10.1063/1.3606642/371638.
[23] T.H. Chen, C.F. Lin, J.Y. Wang, Effects of strain rate on properties of Zr–Cu–Al–Fe bulk metallic glasses with Nb addition, Mater. Chem. Phys. 293 (2023) 126968, https://doi.org/10.1016/j.matchemphys.2022.126968.
[24] C.L. Qiu, Q. Chen, L. Liu, K.C. Chan, A novel Ni-free Zr-based bulk metallic glass with enhanced plasticity and good biocompatibility, Scr. Mater. 55 (2006) 605–608, https://doi.org/10.1016/J.SCRIPTAMAT.2006.06.018.
[25] T.H. Li, P.C. Wong, S.F. Chang, P.H. Tsai, J.S.C. Jang, J.C. Huang, Biocompatibility study on Ni-free Ti-based and Zr-based bulk metallic glasses, Mater. Sci. Eng. C 75 (2017) 1–6, https://doi.org/10.1016/J.MSEC.2017.02.006.
[26] L. Liu, C.L. Qiu, C.Y. Huang, Y. Yu, H. Huang, S.M. Zhang, Biocompatibility of Ni-free Zr-based bulk metallic glasses, Intermetallics 17 (2009) 235–240, https://doi.org/10.1016/J.INTERMET.2008.07.022.
[27] E. Yüce, F. Spieckermann, A. Asci, S. Wurster, P. Ramasamy, L. Xi, B. Sarac, J. Eckert, Toxic element-free Ti-based metallic glass ribbons with precious metal additions, Mater. Today Adv. 19 (2023) 100392, https://doi.org/10.1016/j.mtadv.2023.100392.
[28] A. Reyes-Jara, N. Cordero, J. Aguirre, M. Troncoso, G. Figueroa, Antibacterial effect of copper on microorganisms isolated from bovine mastitis, Front. Microbiol. 7 (2016) 693, https://doi.org/10.3389/FMICB.2016.00626.
[29] T.C.B. Pereira, M.M. Campos, M.R. Bogo, Copper toxicology, oxidative stress and inflammation using zebrafish as experimental model, J. Appl. Toxicol. 36 (2016) 876–885, https://doi.org/10.1002/JAT.3303.
[30] C.N. Cai, C. Zhang, Y.S. Sun, H.H. Huang, C. Yang, L. Liu, ZrCuFeAlAg thin film metallic glass for potential dental applications, Intermetallics 86 (2017) 80–87, https://doi.org/10.1016/j.intermet.2017.03.016.
[31] B. Subramanian, S. Maruthamuthu, S.T. Rajan, Biocompatibility evaluation of sputtered zirconium-based thin film metallic glass-coated steels, Int. J. Nanomedicine 10 (2015) 17–29, https://doi.org/10.2147/IJN.S79977.
[32] Y. Zhang, X. Huang, S. Feng, C. Chen, D. Guo, L. Fang, Platinum accumulation and cancer-related fatigue, correlation with IL-8, TNF-α and hemocytes, Front. Pharmacol. 12 (2021) 658792, https://doi.org/10.3389/FPHAR.2021.658792/BIBTEX.
[33] L. Larsson, J.J. Marattukalam, E.M. Paschalidou, B. Hjörvarsson, N. Ferraz, C. Persson, Biocompatibility of a Zr-based metallic glass enabled by additive manufacturing, ACS Appl. Bio Mater. 5 (2017) 5741–5753, https://doi.org/10.1021/ACSABM.2C00764.
[34] Z. Liu, K.C. Chan, L. Liu, Development of Ni- and Cu-Free Zr-based bulk metallic glasses for biomedical applications, Mater. Trans. 52 (2011) 61–67, https://doi.org/10.2320/matertrans.M2010068.
[35] J. Saida, T. Sanada, S. Sato, M. Imafuku, C. Li, A. Inoue, Nano quasicrystal formation and local atomic structure in Zr-Pd and Zr-Pt binary metallic glasses, Z. Kristallogr. 223 (2008) 726–730, https://doi.org/10.1524/zkri.2008.1041.

[36] P.N. Paqué, M. Özcan, A review on biocompatibility of dental restorative and reconstruction materials, Curr. Oral Health Rep. 11 (2024) 68–77, https://doi.org/10.1007/S40496-023-00358-9.
[37] A. Salminen, K. Kaarniranta, A. Kauppinen, Tissue fibroblasts are versatile immune regulators: an evaluation of their impact on the aging process, Ageing Res. Rev. 97 (2024) 102296, https://doi.org/10.1016/J.ARR.2024.102296.
[38] A. Masood, A. Biswas, V. Ström, L. Belova, J. Ågren, K.V. Rao, The effect of Ni-substitution on physical properties of Fe 72-xB24Nb4Nix bulk metallic glassy alloys, Mater. Res. Soc. Symp. Proc. 1300 (2011) 52–57, https://doi.org/10.1557/OPL.2011.304/METRICS.
[39] D. Turnbull, Under what conditions can a glass be formed? Contemp. Phys. 10 (1969) 473–488, https://doi.org/10.1080/00107516908204405.
[40] Z.P. Lu, C.T. Liu, Glass formation criterion for various glass-forming systems, Phys. Rev. Lett. 91 (2003) 115505, https://doi.org/10.1103/PHYSREVLETT.91.115505/FIGURES/5/MEDIUM.
[41] A. Masood, V. Ström, L. Belova, K.V. Rao, J. Ågren, Effect of Ni-substitution on glass forming ability, mechanical, and magnetic properties of FeBNbY bulk metallic glasses, J. Appl. Phys. 113 (2013) 033904, https://doi.org/10.1063/1.4772753/140118.
[42] C. Suryanarayana, A. Inoue, Bulk metallic glasses: second edition, Bulk Metallic Glasses: Second Edition (2017) 1–520, https://doi.org/10.1201/9781315153483.
[43] G.A. Mansoori, N.F. Carnahan, K.E. Starling, T.W. Leland, Equilibrium thermodynamic properties of the mixture of hard spheres, J. Chem. Phys. 54 (1971) 1523–1525, https://doi.org/10.1063/1.1675048.
[44] J. Bhatt, W. Jiang, X. Junhai, W. Qing, C. Dong, B.S. Murty, Optimization of bulk metallic glass forming compositions in Zr–Cu–Al system by thermodynamic modeling, Intermetallics (Barking) 15 (5–6) (2007) 716–721, https://doi.org/10.1016/J.INTERMET.2006.10.018.
[45] A.R. Miedema, P.F. de Châtel, F.R. de Boer, Cohesion in alloys — fundamentals of a semi–empirical model, Physica B+c 100 (1980) 1–28, https://doi.org/10.1016/0378-4363(80)90054-6.
[46] E. Dastanpour, M.H. Enayati, A. Masood, V. Ström, On the glass forming ability (GFA), crystallization behavior and soft magnetic properties of nanomet-substituted alloys, J. Non Cryst. Solids 529 (2020) 119774, https://doi.org/10.1016/j.jnoncrysol.2019.119774.
[47] B. Ramakrishna Rao, M. Srinivas, A.K. Shah, A.S. Gandhi, B.S. Murty, A new thermodynamic parameter to predict glass forming ability in iron based multi–component systems containing zirconium, Intermetallics 35 (2013) 73–81, https://doi.org/10.1016/J.INTERMET.2012.11.020.
[48] H.Y. Ding, K.F. Yao, High entropy Ti20Zr20Cu20Ni20Be20 bulk metallic glass, J. Non Cryst. Solids 364 (2013) 9–12, https://doi.org/10.1016/J.JNONCRYSOL.2013.01.022.
[49] J. Bhatt, G.K. Dey, B.S. Murty, Thermodynamic and topological modeling and synthesis of Cu–Zr–Ti–Ni-based bulk metallic glasses by mechanical alloying, Metall. Mater. Trans. A Phys. Metall. Mater. Sci. 39 (2008) 1543–1551, https://doi.org/10.1007/S11661-007-9354-8/FIGURES/7.
[50] K. Ackland, A. Masood, S. Kulkarni, P. Stamenov, Ultra-soft magnetic Co–Fe–B–Si–Nb amorphous alloys for high frequency power applications, AIP Adv. 8 (2018) 56129, https://doi.org/10.1063/1.5007707/1025198.
[51] F. Wang, A. Inoue, Y. Han, F.L. Kong, Excellent soft magnetic Fe–Co–B-based amorphous alloys with extremely high saturation magnetization above 1.85 T and low coercivity below 3 A/m, J. Alloys Compd. 711 (2017) 132–142, https://doi.org/10.1016/J.JALLCOM.2017.03.341.
[52] A. Inoue, Stabilization of metallic supercooled liquid and bulk amorphous alloys, Acta Mater. 48 (2000) 279–306, https://doi.org/10.1016/S1359-6454(99)00300-6.
[53] M.X. Li, Y. Sun, C. Wang, Y. Liu, Data-driven discovery of a universal indicator for metallic glass forming ability, Nat. Mater. 21 (2021) 165–172, https://doi.org/10.1038/s41563-021-01129-6.
[54] P. Zhang, J.J. Maldonis, Z. Liu, J. Schroers, P.M. Voyles, Spatially heterogeneous dynamics in a metallic glass forming liquid imaged by electron correlation microscopy, Nat. Commun. 9 (2018) 963, https://doi.org/10.1038/s41467-018-03604-2.
[55] J. Saida, M. Matsushita, C. Li, A. Inoue, Formation of icosahedral quasicrystalline phase in $Zr_{70}Ni_{10}M_{20}$(M=Pd, Au, Pt) ternary metallic glasses, Appl. Phys. Lett. 76 (2000) 3558–3560, https://doi.org/10.1063/1.126706.
[56] D.V. Louzguine-Luzgin, A. Inoue, An extended criterion for estimation of glass-forming ability of metals, J. Mater. Res. 22 (2007) 1378–1383, https://doi.org/10.1557/JMR.2007.0167/METRICS.
[57] J.P. Liao, B.J. Yang, Y. Zhang, W.Y. Lu, X.J. Gu, J.Q. Wang, Evaluation of glass formation and critical casting diameter in Al-based metallic glasses, Mater. Des. 88 (2015) 222–226, https://doi.org/10.1016/J.MATDES.2015.08.138.
[58] K.M. Han, H. Jiang, Y.M. Wang, J.B. Qiang, Zr–Ti–Al–Fe–Cu bulk metallic glasses for biomedical device application, Rare Met. 40 (2021) 1239–1246, https://doi.org/10.1007/s12598-020-01644-6.
[59] J.K. Stalick, R.M. Waterstrat, The zirconium-platinum phase diagram, J. Alloys Compd. 430 (2007) 1–2, https://doi.org/10.1016/J.JALLCOM.2006.04.055.
[60] M. Lomello-Tafin, P. Galez, J.C. Gachon, P. Feschotte, J.L. Jorda, The Zr–Au system, J. Alloys Compd. 257 (1997) 215–223, https://doi.org/10.1016/S0925-8388(96)03124-6.
[61] S. Bera, P. Ramasamy, D. Şopu, B. Sarac, J. Zálešák, Ch. Gammer, M. Stoica, M. Calin, J. Eckert, Tuning the glass forming ability and mechanical properties of Ti–based bulk metallic glasses by Ga additions, J. Alloys Compd. 793 (2019) 552–563, https://doi.org/10.1016/J.JALLCOM.2019.04.173.
[62] M.A. Suárez, R. Esquivel, J. Alcántara, H. Dorantes, J.F. Chávez, Effect of chemical composition on the microstructure and hardness of Al–Cu–Fe alloy, Mater Charact 62 (2011) 917–923, https://doi.org/10.1016/J.MATCHAR.2011.06.009.
[63] "M.G. Scott, 'Amorphous Metallic Alloys' in F.E. Luborsky (Ed.) Butterworths, London, 1983, p.144-160.
[64] F. Sourani, K. Raeissi, M.H. Enayati, M. Kharaziha, A. Hakimizad, G. Blugan, H. R. Salimijazi, Corrosion and tribocorrosion behavior of ZrO_2–Al_2O_3 composite coatings developed by plasma electrolytic oxidation for load-bearing implants, J. Alloys Compd. 920 (2022) 165856, https://doi.org/10.1016/J.JALLCOM.2022.165856.
[65] B.R. Chen, Y.R. Police, M. Li, P.R. Chinnam, T.R. Tanim, E.J. Dufek, A mathematical approach to survey electrochemical impedance spectroscopy for aging in lithium-ion batteries, Front. Energy Res. 11 (2023) 1132876, https://doi.org/10.3389/FENRG.2023.1132876/.
[66] M.R. Shoar Abouzari, F. Berkemeier, G. Schmitz, D. Wilmer, On the physical interpretation of constant phase elements, Solid State Ion. 180 (2009) 922–927, https://doi.org/10.1016/J.SSI.2009.04.002.
[67] L. Huang, Y. Yokoyama, W. Wu, P.K. Liaw, S. Pang, A. Inoue, T. Zhang, W. He, Ni–free Zr–Cu–Al–Nb–Pd bulk metallic glasses with different Zr/Cu ratios for biomedical applications, J. Biomed. Mater. Res. B Appl. Biomater. 100 (2012) 1472–1482, https://doi.org/10.1002/JBM.B.32715.
[68] Q. Shao, Q. Zhang, J. Zhang, Y. Zhang, T. Li, One-step fabrication of bimetallic PtPd mesoporous nanospheres for methanol electrooxidation, SSRN Electron. J. (2022) 3977557, https://doi.org/10.2139/SSRN.3977557.
[69] X. Lyu, W.-N. Zhang, G. Li, B.-W. Shi, Y.-N. Zhang, H. Chen, S.-C. Li, X. Wang, Two–dimensional porous PtPd nanostructure electrocatalysts for oxygen reduction reaction, ACS Appl. Nano Mater. 3 (2020) 8586–8591, https://doi.org/10.1021/ACSANM.0C01900.
[70] M.M. Khan, I. Shabib, W. Haider, A combinatorially developed Zr–Ti–Fe–Al metallic glass with outstanding corrosion resistance for implantable medical devices, Scr. Mater. 162 (2019) 223–229, https://doi.org/10.1016/j.scriptamat.2018.11.011.
[71] Z. Liu, G.Q. Zhang, F. Gao, C.Z. Wang, Novel low Cu content and Ni-free Zr-based bulk metallic glasses for biomedical applications, J. Non Cryst. Solids 363 (2013) 1–5, https://doi.org/10.1016/j.jnoncrysol.2012.09.026.
[72] Z. Zhang, X. Zhong, X. Teng, Y. Huang, H. Han, T. Chen, Q. Zhang, X. Yang, Y. Gong, Effect of annealing temperature on electrochemical properties of $Zr_{56}Cu_{19}Ni_{11}Al_9Nb_5$ in PBS solution, Materials 16 (2023) 3389, https://doi.org/10.3390/ma16093389.
[73] W.H. Jiang, F. Jiang, B.A. Green, F.X. Liu, P.K. Liaw, H. Choo, K.Q. Qiu, Electrochemical corrosion behavior of a Zr-based bulk-metallic glass, Appl. Phys. Lett. 91 (2007) 041907, https://doi.org/10.1063/1.2762282.
[74] L. Liu, C.L. Qiu, H. Zou, K.C. Chan, The effect of the microalloying of Hf on the corrosion behavior of ZrCuNiAl bulk metallic glass, J. Alloys Compd. 399 (2005) 144–148, https://doi.org/10.1016/j.jallcom.2005.03.016.
[75] Y. Chen, S.I. Roohani-Esfahani, Z.F. Lu, H. Zreiqat, C.R. Dunstan, Zirconium ions Up-regulate the BMP/SMAD signaling pathway and promote the proliferation and differentiation of human osteoblasts, PLoS One 10 (2015) e0113426, https://doi.org/10.1371/JOURNAL.PONE.0113426.
[76] A.J. Theron, G.J. Ramafi, C. Feldman, H. Grimmer, S.S. Visser, R. Anderson, Effects of platinum and palladium ions on the production and reactivity of neutrophil-derived reactive oxygen species, Free Radic. Biol. Med. 36 (2004) 1408–1417, https://doi.org/10.1016/J.FREERADBIOMED.2004.02.064.
[77] A. Larsen, K. Kolind, D.S. Pedersen, P. Doering, M.O. Pedersen, G. Danscher, M. Penkowa, M. Stoltenberg, Gold ions bio-released from metallic gold particles reduce inflammation and apoptosis and increase the regenerative responses in focal brain injury, Histochem. Cell Biol. 130 (2008) 681–692, https://doi.org/10.1007/S00418-008-0448-1.
[78] E. Martín-Vázquez, N. Cobo-Vuilleumier, L. López-Noriega, P.I. Lorenzo, B. R. Gauthier, The PTGS2/COX2-PGE_2 signaling cascade in inflammation: pro or anti? A case study with type 1 diabetes mellitus, Int. J. Biol. Sci. 19 (2023) 4157–4165, https://doi.org/10.7150/IJBS.86492.